PRE-PRINT ARTICLE

COPYRIGHT BY COMPOSITES THEORY AND PRACTICE JOURNAL

ISSN: 2299-128X

Influence of reinforcement volume fraction on Ni phase formation and mechanical properties in alumina-metal composites

Justyna Zygmuntowicz[1,*], Katarzyna Konopka[1], Marek Krasnowski[1], Paulina Piotrkiewicz[1], Marcin Wachowski[2], Ireneusz Szachogłuchowicz[2], Paweł Falkowski[3]

[1]Warsaw University of Technology, Faculty of Materials Science and Engineering, 141 Woloska St., 02-507 Warsaw, Poland

[2]Military University of Technology, Faculty of Mechanical Engineering, 2 gen. S. Kaliskiego St., 00-908 Warsaw, Poland

[3]Faculty of Chemistry, Warsaw University of Technology, 3 Noakowskiego St., 00-664 Warsaw, Poland

https://doi.org/10.62753/ctp.2026.04.1.1

Abstract

This work reports on the fabrication and characterization of Al_2O_3-based composites reinforced with NiAl + 30 wt% Al_2O_3 pre-alloyed powder, synthesized via mechanical alloying. Two composite series were prepared using slip casting: Series I with 2.5 vol.% and Series II with 5.0 vol.% of the reinforcement phase. The samples were sintered at 1450°C in a reducing H_2/N_2 atmosphere. X-ray diffraction revealed that, in both series, after sintering, no NiAl was observed; only Ni was detected. SEM and EDS analyses showed uniform dispersion of the reinforcement. Mechanical testing revealed that increasing the metallic phase reduced the hardness from 17.01 ± 0.61 GPa (Series I) to 15.73 ± 1.51 GPa (Series II), while the fracture toughness slightly improved from 5.14 ± 0.30 to 5.20 ± 0.37 MPa·$m^{0.5}$. The compressive strength reached 25 kN and 17 kN for Series I and II, respectively. The results demonstrate that a tailored reinforcement content enables control over the microstructure and mechanical performance in Al_2O_3-NiAl composites.

Keywords: composites, mechanical alloying, slip casting, NiAl-Al_2O_3 composite powder, fracture toughness

Introduction

Ceramic matrix composites constitute an important group of engineering materials. Among them are ceramic-intermetallic composites. Combining both materials, ceramics and an intermetallic phase, yields a new material with the desired properties, including high hardness, good bending strength, improved fracture toughness, the

* Corresponding author: Justyna.zygmuntowicz@pw.edu.pl

PRE-PRINT ARTICLE

COPYRIGHT BY COMPOSITES THEORY AND PRACTICE JOURNAL

ISSN: 2299-128X

Polish Society of Composite Materials

ability to work at elevated temperatures, and other characteristics of the intermetallic phase, such as electrical properties [1-2]. Such composites are highly desired in many engineering applications, for example, as ball roller bearings, parts of jet engine turbines, connecting roads, various parts in aerospace engineering, and others [3-4].

Al_2O_3 ceramics are often selected as matrices for composites. As an intermetallic phase, NiAl [5-6], Ni_3Al [7], TiAl [8], or TiC [10] is used. The intermetallic phase is mostly distributed in the matrix as particles, which are active in processes such as crack deflection, bridging, and others [10]. The highest enhancement of fracture toughness, together with the hardening effect, is achieved in complex structures with distributed ceramic-matrix micro- and nanosized reinforcement particles [11]. Such composites can be produced by methods based on powder consolidation [12]. In these techniques, various sizes of ceramic and reinforcement powders can be used. However, the most crucial technological challenge is the fabrication of composite structures with various micro- and nanosized reinforcement particles in a controlled distribution. The location of reinforcement particles differs in size: separate particles surrounded by ceramic grains, as well as at grain boundaries and triple points, are required to achieve the synergistic effect of improving the mechanical properties of composites [9].

The complex structure can be produced by using reinforcement in the form of a composite powder. We proposed using NiAl-Al_2O_3 as a reinforcement composite powder, prepared by the mechanical alloying of Ni, Al, and Al_2O_3 powders [5, 13-15]. Such composite powders, consolidated with the addition of Al_2O_3 as the matrix, resulted in a bulk composite material Al_2O_3-(NiAl-Al_2O_3) with microstructures consisting of ceramic matrix grains and reinforcement particles of two phases, NiAl and Al_2O_3 [5, 13-15]. The composite's complex structure is characterized by fine NiAl particles dispersed in the ceramic matrix and ceramic particles trapped within it, as shown in Figure 1.

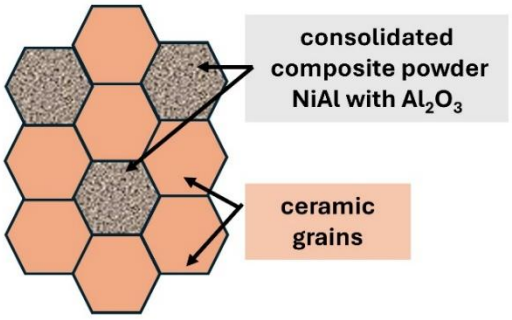

Figure 1. Diagram of composite microstructure made by consolidation of reinforcement composite powder (NiAl - Al_2O_3) with Al_2O_3 matrix powder.

PRE-PRINT ARTICLE

COPYRIGHT BY COMPOSITES THEORY AND PRACTICE JOURNAL

ISSN: 2299-128X

Polish Society of Composite Materials

Various powder consolidation techniques determine the size and distribution of reinforcement particles in the ceramic matrix, as well as the grain size and phase composition of the ceramic [16-17]. Pulse plasma sintering (PPS) enables rapid sintering and prevents ceramic grain growth [13-15, 18-19]. Another very popular method, slip casting, produces homogeneous, dense materials [20-22]. Nevertheless, depending on the atmosphere during sintering, the phase composition of the composite can be modified [23-24]. As an example, in the Ni-Al_2O_3 system, sintering in air results in the formation of the spinel phase $NiAl_2O_4$ [25]. In such a case, a multiphase composite with a complex structure can be formed. Previous results of the authors' own experimental work revealed that NiAl-Al_2O_3 composite powder, together with Al_2O_3 powder consolidated by the slip casting method and sintered in air, results in a high density composite with favorable mechanical properties [26]. The phase composition of the composite consisted of Al_2O_3, Ni, and $NiAl_2O_4$. The complex structure was observed and characterized by fine Al_2O_3 particles located in Ni areas, surrounded by Al_2O_3 ceramic grains, as well as by spinel particles [5].

The present work focuses on Al_2O_3-based composites reinforced with mechanically alloyed NiAl + Al_2O_3 powders, a class of materials with a potential for high performance structural and functional applications. By investigating both the phase evolution and mechanical response, the study provides insights into how to control the balance between hardness and fracture toughness in oxide-metal systems. Moreover, the research presented in the work reveals the critical role of the sintering atmosphere. Previous studies (including the authors' own) have shown that air sintering leads to the formation of $NiAl_2O_4$ spinel, thereby improving the fracture toughness. In this investigation, a reducing N_2/H_2 atmosphere suppresses spinel formation and stabilizes metallic Ni, leading to distinct microstructures and properties. This demonstrates how atmosphere engineering can be used as a processing lever to tune composite performance.

In the paper, the fabrication of an Al_2O_3 + (NiAl + 30 wt% Al_2O_3) composite from initial NiAl-Al_2O_3 and Al_2O_3 composite powders by slip casting and sintering in a N_2/H_2 atmosphere is presented. The study compares composites with different reinforcement contents (2.5 vs. 5 vol.%). The work clearly shows how reinforcement fraction and phase stability (Ni vs. $NiAl_2O_4$) impact hardness, toughness, and compressive strength. These relationships are crucial for designing materials for structural applications.

In addition, the research presented in this work expands the scope of mechanical testing for this type of composite. Beyond hardness and fracture toughness, the study includes compressive strength tests by means of digital image correlation (DIC). This provides a fuller picture of the load-bearing capacity and failure mechanisms, which are rarely reported for such systems.

PRE-PRINT ARTICLE

COPYRIGHT BY COMPOSITES THEORY AND PRACTICE JOURNAL

ISSN: 2299-128X

Polish Society of Composite Materials

Materials and methods

α-Al_2O_3 powder (TM-DAR, Taimei Chemicals Co., Ltd., Tokyo, Japan), characterized by an average particle diameter of 0.1 μm, a high purity level of 99.99%, and a theoretical density of 3.9 g/cm³, was used to produce the ceramic matrix in the fabricated composites. To produce the composite powder containing the intermetallic phase NiAl and 30 wt% Al_2O_3, hereinafter referred to as the pre-composite powder (used in the further part of the experiment for the production of composites), two types of metallic powders (Al and Ni) and Al_2O_3, different than that used for the matrix (Almatis), were used. The aluminum powder (ABCR GmbH & Co. KG, Karlsruhe, Germany) has a nominal particle size of 44 μm, a theoretical density of 2.7 g/cm³, and a purity of 99.7%. The second metallic phase was nickel powder, sourced from ABCR GmbH & Co. KG (Karlsruhe, Germany), with a particle size distribution of 3-7 μm and a density of 8.9 g/cm³. At the same time, the Al_2O_3 A16SG (Almatis) powder has an average particle size equal to 0.5 ±0.1 μm and a density of 3.90 g/cm^3. The suspension formulations included diammonium hydrocitrate (DAC) and citric acid (CA), both obtained from Sigma-Aldrich (Poland), as dispersing agents. Deionized water served as the liquid medium for slurry preparation.

The preliminary stage of the study involved mechanical alloying to produce a composite powder comprising the NiAl intermetallic phase and 30 wt% Al_2O_3, hereafter referred to as the pre-composite powder. The alloying process was performed using a SPEX 8000D high-energy shaker mill (SPEX® SamplePrep, Metuchen, NJ, USA). The powder mixture containing the elemental Ni and Al in a 1:1 atomic ratio, along with 30 wt% α-Al_2O_3, was subjected to milling. The powder blend was processed at a ball-to-powder mass ratio of 8:1 under an inert argon atmosphere to prevent oxidation during high-energy milling.

Using the pre-composite powders, the composites were produced via slip casting. The multi-step fabrication process included preparing slurries of Al_2O_3 powder and the NiAl-30 Al_2O_3 pre-composite powder from the previous stage of the experiment. The powders were combined with a solvent and a plasticizer to obtain a slurry. Distilled water was used as the solvent, while the plasticizers were diammonium hydrogen citrate and citric acid. The plasticizers were added to the slurry at 0.3% and 0.1% by weight, respectively, relative to the total weight of the powders. The premixed slurry was then subjected to homogenization in a Retsch PM400 planetary ball mill for 1 h at 300 rpm. After this time, it was mixed and deaerated in a Thinky ARE-250 high-speed planetary mixer. Mixing was carried out for 5 min at 2000 rpm, and deaeration for 3 min at 2200 rpm. The slurry prepared as above was cast into plastic molds on a gypsum plate. The obtained green bodies were dried in a laboratory dryer at 40°C for 24 hours to remove any remaining solvent, and then sintered.

The sintering process was carried out at 1450°C using an H_2/N_2 reducing atmosphere. The heating process was carried out in two stages, from 0°C to 150°C at a 5°C/min heating rate, then from 150°C to 1450°C at a 2°C/min

PRE-PRINT ARTICLE
COPYRIGHT BY COMPOSITES THEORY AND PRACTICE JOURNAL
ISSN: 2299-128X
Polish Society of Composite Materials

heating rate. The holding time at the sintering temperature was 2 h. Following the procedure described above, two series of Al_2O_3 matrix composite samples with 2.5 vol.% (Series I) and 5 vol.% (Series II) NiAl + 30 wt% Al_2O_3 pre-composite powder were fabricated and characterized. The composites were sintered in a mixed H_2/N_2 atmosphere to provide a controlled reducing environment. Hydrogen ensures a low oxygen partial pressure, preventing the oxidation of Ni and suppressing $NiAl_2O_4$ spinel formation, while nitrogen acts as an inert carrier gas that moderates the reducing strength, stabilizes the atmosphere, and enables safe furnace operation. The H_2/N_2 mixture, therefore, maintains conditions under which NiAl decomposes to metallic Ni without forming oxide phases.

Table 1. Compositions of prepared slurries.

Component	Alumina oxide (Al_2O_3)	NiAl + 30 wt% Al_2O_3	Citric acid (CA)	Diammonium hydrocitrate (DAC)	Water (H_2O)
Proportion	Vol.%	Vol.% with respect to the amount of ceramic	Wt% with respect to the amount of ceramic or ceramic and metal powders.		Vol.%
Series I	2.5	5	0.1	0.3	50
Series II	47.5	45			

The actual density of the NiAl + 30 wt% Al_2O_3 pre-composite powder after mechanical alloying for 18 hours was determined using a helium gas pycnometer (AccuPyc II 1340, Micromeritics Instrument Corporation, Norcross, GA, USA). This method is based on the gas displacement technique, which enables precise measurement of the true volume occupied by the solid phase, excluding interparticle voids and open porosity. Prior to measurement, the powder samples were dried to remove adsorbed moisture, and the chamber was purged with helium to ensure accurate measurements. The measurements were conducted in accordance with the guidelines outlined in the ASTM D3766 standard [27], which provides protocols for the use of gas pycnometers to determine the density of particulate materials. A series of consecutive measurements was performed for each sample to ensure statistical reliability, and the reported density values represent the mean of the consistent measurements.

The phase composition of the powders after mechanical alloying (MA) and the fabricated composite samples was examined by X-ray diffraction (XRD). The measurements were performed utilizing a Rigaku MiniFlex II diffractometer (Rigaku Corporation, Tokyo, Japan) equipped with a Cu Kα radiation source (λ = 1.54178 Å). The instrument operated at an accelerating voltage of 30 kV and a current of 15 mA. XRD data were collected

PRE-PRINT ARTICLE
COPYRIGHT BY COMPOSITES THEORY AND PRACTICE JOURNAL
ISSN: 2299-128X
Polish Society of Composite Materials

in the step-scanning mode over a 2θ range of 23° to 120°, enabling comprehensive detection of diffraction peaks from the crystalline phases. The scan parameters included a step size of 0.05° and a counting time of 3 seconds per step, ensuring sufficient resolution and signal intensity for qualitative and semi-quantitative phase identification.

The mean crystallite size of the NiAl phase obtained after mechanical alloying was estimated by means of Williamson-Hall (W-H) analysis [28-29], a method that accounts for both the crystallite size and lattice strain contributions to the broadening of X-ray diffraction peaks. This approach provides a more accurate evaluation than the Scherrer equation alone, particularly for mechanically alloyed materials where strain effects can be significant. To apply the W-H method, the integral breadth (β) of each selected diffraction peak was measured and corrected for instrumental broadening [31]. The instrumental contribution was determined using a standard reference material with negligible broadening (such as silicon or LaB_6), and subtracted from the measured full width at half maximum (FWHM) values to yield the physical broadening attributable to the sample. The corrected β values were then used in the Williamson-Hall equation: $\beta cos\theta = \frac{k \cdot \lambda}{D} + 4\epsilon sin\theta$, where: β is the physical broadening (in radians), θ is the Bragg angle, k is the shape factor (typically ~0.9), λ is the X-ray wavelength (1.54178 Å for CuKα radiation), D is the average crystallite size, ϵ is the microstrain in the lattice. A linear plot of βcosθ versus sinθ was constructed, and crystallite size D was extracted from the y-intercept of the fitted line [28-31]. The slope of the line provided an estimate of lattice strain ϵ. This method enabled reliable assessment of the nanocrystalline structure of the NiAl phase formed during mechanical alloying.

The microstructural features of both the mechanically alloyed powder and the sintered composite samples were examined employing scanning electron microscopy (SEM). The observations were carried out on a JEOL JSM-6610 scanning electron microscope (JEOL Ltd., Tokyo, Japan), which is equipped with both secondary electron (SE) and backscattered electron (BSE) detectors. The SE imaging mode was primarily utilized to reveal surface topography and particle morphology, while the BSE mode provided compositional contrast, highlighting the phase distribution based on atomic number differences. All the SEM analyses were conducted at an accelerating voltage of 15 kV, which provided sufficient resolution and penetration for imaging both fine particles and consolidated ceramic-metal structures. The working distance and detector settings were optimized to ensure high-quality micrographs of the powder particles and sintered microstructures. To complement the imaging and gain insight into the chemical composition, energy dispersive X-ray spectroscopy (EDS) was employed. A high-resolution X-Max EDS detector (Oxford Instruments, Oxford, UK) integrated with the SEM system was used for qualitative and semi-quantitative elemental analysis. Surface microanalysis was performed on the mechanically alloyed powder to verify the successful formation and homogeneity of the NiAl phase. Additionally, EDS mapping and point analyses were conducted on sintered samples prepared by slip casting to assess the distribution and concentrations of constituent elements, particularly aluminum, nickel,

PRE-PRINT ARTICLE
COPYRIGHT BY COMPOSITES THEORY AND PRACTICE JOURNAL
ISSN: 2299-128X
Polish Society of Composite Materials

and oxygen. The combined use of SEM and EDS provided a comprehensive understanding of the morphological and compositional characteristics of the materials at various processing stages.

The Vickers hardness of the sintered composite samples was measured employing a microindentation technique on polished cross-sections of each specimen. The tests were carried out by means of an HVS-30T hardness tester (Huatec Group Corporation, Beijing, China), applying a load of 10 kgf (98.07 N) with a dwell time of 10 seconds. The indentation imprints were carefully examined under a Nikon Eclipse LV150N light microscope (Nikon Corporation, Tokyo, Japan) to determine the diagonal lengths of the impressions. The hardness values were calculated according to the standard Vickers formula: $HV = \frac{1.8544 \cdot F}{d^2}$, where F is the applied load (in kgf), and d is the average diagonal length of the indentation (in mm). To ensure statistical reliability, a minimum of ten indentations were performed on each sample, and the average value was reported. For Vickers hardness testing, the ISO 6507 [32] standard was used.

The fracture toughness (K_{IC}) was evaluated utilizing the indentation fracture method, which estimates toughness based on the radial cracks emanating from the corners of the Vickers indentations. This method provides a comparative evaluation of crack resistance in brittle materials. The fracture toughness was calculated using the widely accepted Anstis equation [33-34]: $K_{IC} = 0.016\left(\frac{E}{HV}\right)^{0.5} \cdot \frac{F}{c^{1.5}}$, where E - Young's modulus; HV - Vickers hardness; F - total load applied; c - central crack length.

The crack lengths were measured employing the same light microscope equipped with calibrated software. This method enabled comparative evaluation of the fracture toughness between samples with different compositions and microstructures.

Monotonic compression tests were performed to evaluate the mechanical response and failure behavior of the composite samples under uniaxial compressive loading. The experiments were conducted by means of a servo-hydraulic testing machine (Instron 8802, Instron, Norwood, MA, USA), which is capable of delivering high-precision, high-load testing conditions. This apparatus was selected for its ability to apply controlled, continuous compressive loads, accurately simulating real-world mechanical stress scenarios. The Instron 8802 system was equipped with dedicated software that allowed real-time acquisition of load and displacement data. The displacement of the compression plate was continuously recorded, generating a displacement curve that enabled identification of the elastic, plastic, and failure regions during the test. To monitor the deformation behavior of the samples with high spatial and temporal resolution, a digital image correlation (DIC) system was integrated into the test setup. The DIC system consisted of high-speed cameras (operating at acquisition frequencies exceeding 100,000 Hz) strategically positioned around the sample. Prior to testing, the surface of each specimen was prepared with a random high-contrast speckle pattern, which enabled accurate strain measurements via DIC. During testing, the DIC system captured sequential images of the specimen surface,

PRE-PRINT ARTICLE
COPYRIGHT BY COMPOSITES THEORY AND PRACTICE JOURNAL
ISSN: 2299-128X
Polish Society of Composite Materials

which were then processed with specialized DIC software to compute full-field strain maps. These maps provided real-time visualization of the surface strain distribution, allowing the identification of strain localization zones, crack initiation points, and the progression of failure mechanisms as the compressive load increased. Compression was applied monotonically at a constant displacement rate until catastrophic failure occurred. The synchronized operation of the Instron 8802 system and the DIC enabled the integration of mechanical (load-displacement) and optical (strain-field) data. The load-displacement curves obtained from the Instron machine illustrated the global mechanical response, while the DIC strain fields revealed the local deformation characteristics, providing critical insight into the material's failure behavior. During monotonic compression testing, a constant displacement rate was used, where loading was applied under displacement control. The test was continued until catastrophic failure, and mechanical data acquisition was synchronized with the DIC system.

This combined methodology provided a comprehensive evaluation of the compressive strength, deformation behavior, and fracture mechanisms of the tested composites, enhancing the understanding of their performance under uniaxial compressive loading.

A quantitative evaluation of the composite samples' microstructure was conducted using MicroMeter v.086b image analysis software [35-38]. This computer-assisted analysis was applied to determine the morphological and dimensional characteristics of the Al_2O_3 grains embedded in the composite matrix, following procedures established in previous studies [35-38]. The microstructural analysis was performed on high-resolution SEM micrographs acquired from fractured surfaces of the sintered samples. Images were taken from randomly selected areas to ensure statistical representativeness and minimize bias from local microstructural inhomogeneities. A minimum of fifteen fields per sample were analyzed under identical magnification and imaging conditions. The measured values allowed the mean grain size to be determined and grain-size distribution histograms to be made. The obtained quantitative data offer insight into the actual dimensional characteristics of the Al_2O_3 phase in the composite, which can be correlated with the mechanical properties and fracture behavior.

Results

To synthesize the NiAl + 30 wt% Al_2O_3 powder, three commercially available powders were used as the starting materials; SEM micrographs of these powders are shown in Figure 2.

The nickel powder was supplied by ABCR GmbH & Co. KG. The SEM micrographs (Figure 2a) show that the Ni particles possess a highly developed, dendritic-like morphology with a rough surface texture. Based on the observations, the average particle size is 2-10 μm, although the complex morphology can make precise

PRE-PRINT ARTICLE

COPYRIGHT BY COMPOSITES THEORY AND PRACTICE JOURNAL

ISSN: 2299-128X

Polish Society of Composite Materials

sizing challenging. Most probably, the specific surface area is relatively high due to the extensive surface roughness, which can facilitate diffusion during mechanical alloying.

The aluminum powder (Figure 2b) was also sourced from ABCR GmbH & Co. KG. As shown in Figure 2b, the Al particles are irregularly shaped, plate-like, and exhibit a broad particle size distribution. The particles range from approximately 20 μm to over 100 μm in length and have relatively smooth surfaces compared to the Ni powder. The flake-like structure of the Al particles is typical for commercially available aluminum powders and plays a critical role in enhancing cold welding and layer formation during mechanical alloying, which is essential for promoting intermetallic formation.

The reinforcing phase, Al_2O_3 powder (Figure 2c), was provided by Almatis. The SEM analysis (Figure 2c) reveals that the alumina particles are very fine, equiaxed, and nearly spherical or subangular in shape. The primary particle size is in the submicron range, typically 100-1000 nm. The fine, uniform morphology of the Al_2O_3 powder ensures even dispersion within the metallic matrix during mechanical alloying. This high surface area and small particle size enhance the effectiveness of Al_2O_3 as a reinforcing phase by increasing interfacial bonding and load transfer efficiency.

PRE-PRINT ARTICLE

COPYRIGHT BY COMPOSITES THEORY AND PRACTICE JOURNAL

ISSN: 2299-128X

Polish Society of Composite Materials

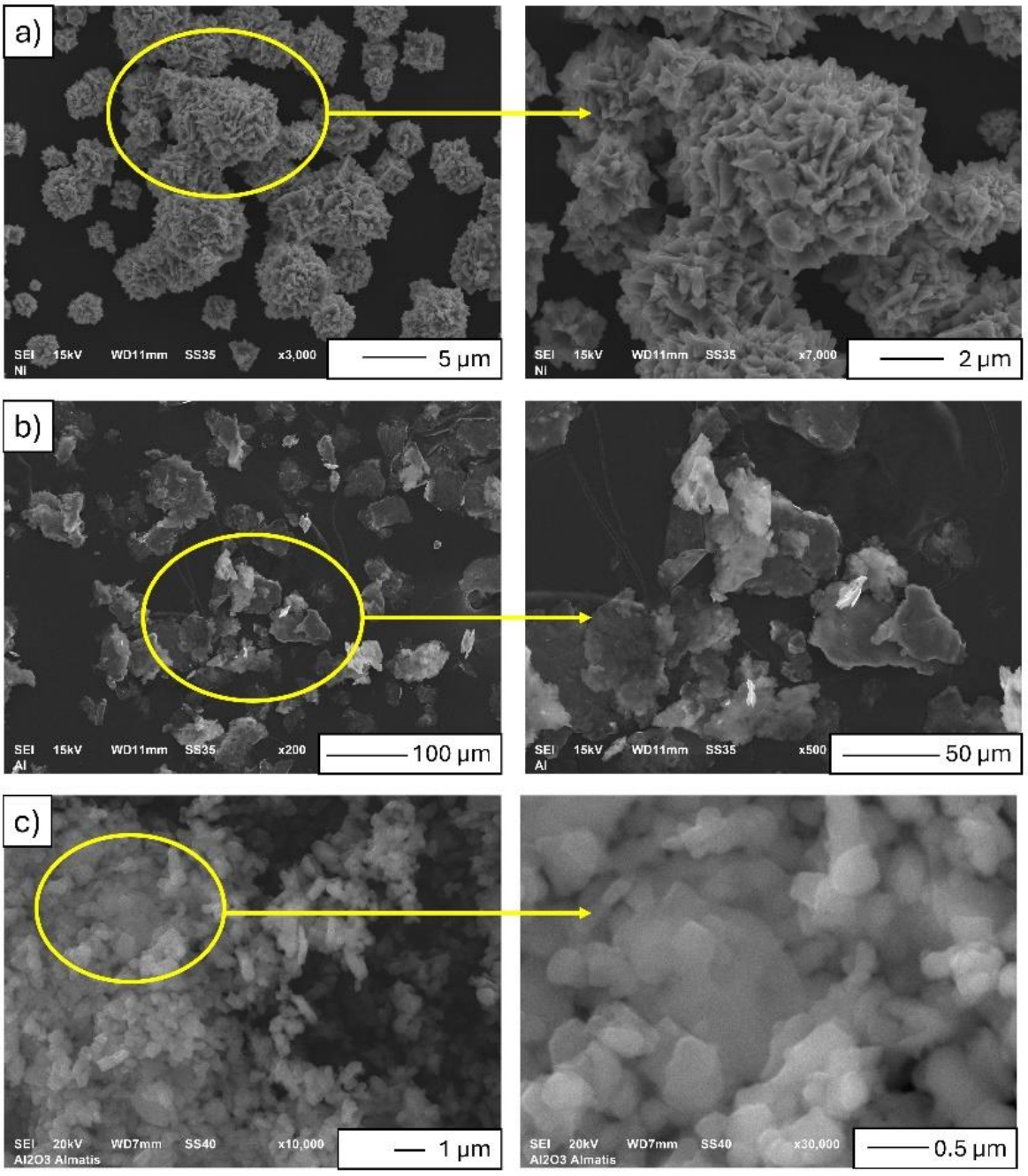

Figure 2. SEM micrographs of powders used to produce NiAl + 30 wt% Al_2O_3 powder: a) Ni (ABCR GmbH & Co. KG, b) Al (ABCR GmbH & Co. KG), c) Al_2O_3 (Almatis).

The ceramic matrix component of the fabricated composite was based on high-purity α-Al_2O_3 powder designated as TM-DAR, supplied by Taimei Chemicals Co., Ltd. This powder is well known for its ultrafine particle size, high sinterability, and uniform morphology, making it a preferred choice for advanced ceramic and composite applications.

PRE-PRINT ARTICLE

COPYRIGHT BY COMPOSITES THEORY AND PRACTICE JOURNAL

ISSN: 2299-128X

Polish Society of Composite Materials

SEM micrographs acquired at magnifications of 20,000× and 30,000× (Figure 3) reveal that the Al_2O_3 (TM-DAR) powder consists of nanoscale, near-spherical primary particles, which exhibit a relatively narrow size distribution (Figure 3). The individual particles have an average size of approximately 100 to 300 nm. These nanosized particles tend to form agglomerates, which are clearly visible in the micrographs as loosely packed clusters. The agglomerates are composed of smaller particles held together by weak interparticle forces, such as van der Waals forces, which are broken down during mechanical processing (planetary ball milling). The powder exhibits a homogeneous microstructure, with no evidence of coarse particles or irregular fragments, indicating a high degree of uniformity and consistency in the manufacturing process. The overall morphology is globular, with a smooth surface texture typical of high-purity nanopowders synthesized via chemical precipitation or hydrothermal routes.

The nanometric size of the TM-DAR particles is particularly advantageous for composite fabrication. It improves the dispersion of the ceramic phase within the metallic or intermetallic matrix during mechanical alloying and enhances the sintering kinetics during subsequent thermal treatments. The high specific surface area of the Al_2O_3 particles also promotes strong interfacial bonding, which is critical for achieving optimal load transfer and mechanical integrity in the final composite material.

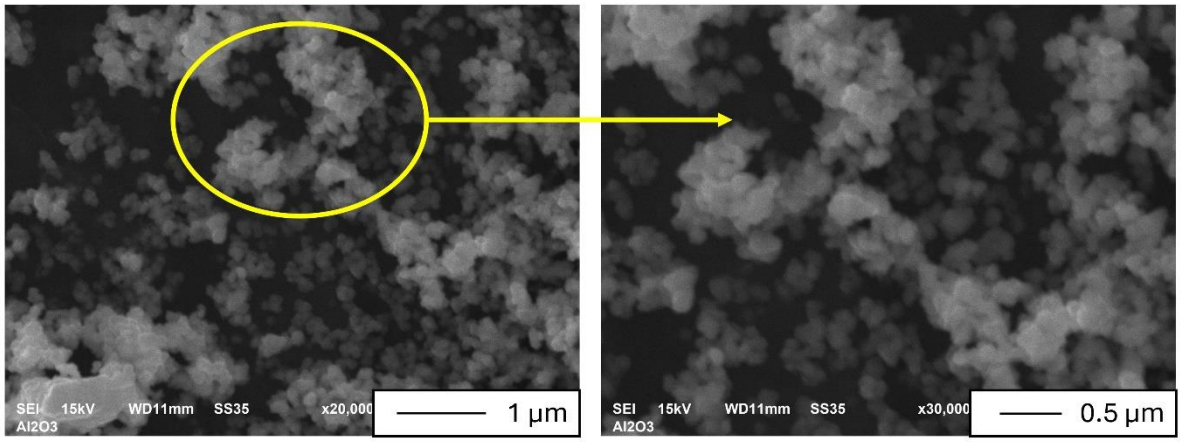

Figure 3. SEM micrographs of Al_2O_3 (TM-DAR) powder used as ceramic matrix for fabricating composites via slip casting.

In the next step, XRD was carried out to determine the phase composition of the powder obtained by mechanical synthesis.

The XRD studies show (Figure 4) that during the milling of the Al-Ni-Al_2O_3 powder mixture, a reaction between Al and Ni occurred, resulting in the formation of an NiAl intermetallic phase. This intermetallic phase and Al_2O_3 ceramics were present in the milling product after 18 h of the process. The produced NiAl phase

PRE-PRINT ARTICLE
COPYRIGHT BY COMPOSITES THEORY AND PRACTICE JOURNAL
ISSN: 2299-128X

had a nanocrystalline structure with a mean crystallite size (estimated by the Williamson-Hall method) of 11 nm. Figure 5 presents the Williamson-Hall plot for the NiAl phase after 18 h of mechanical alloying.

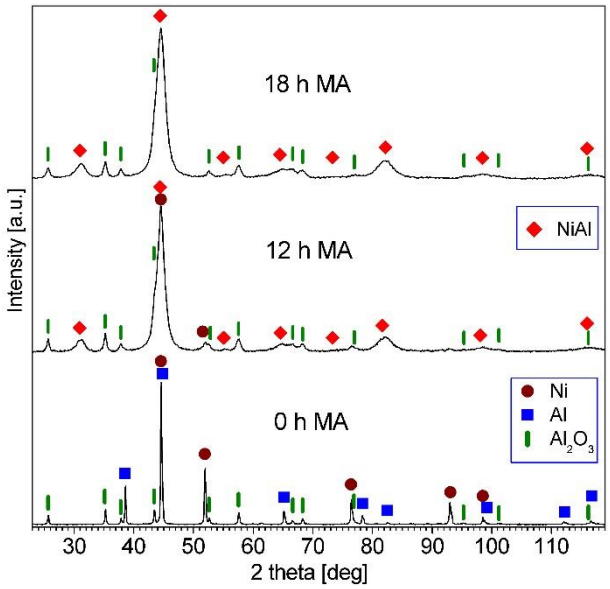

Figure 4. XRD patterns of Al-Ni-Al_2O_3 powder mixture at various milling times.

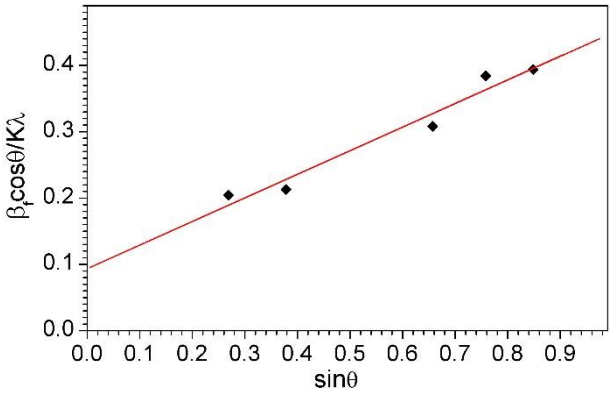

Figure 5. Williamson-Hall plot for NiAl intermetallic phase.

In the next stage of the research, the chemical composition of the powder obtained after the 18-hour mechanical synthesis was examined, and used in the subsequent stage to form composites using the slip casting method. The top-left image (Figure 6) presents an SEM micrograph acquired at 15 kV accelerating voltage and 5500× magnification. The micrograph reveals agglomerates of submicron scale particles with a rough, cauliflower-like morphology. Three areas (labelled #1, #2, and #3) have been marked with yellow squares, indicating the regions selected for EDS analysis of area E (the results are presented in Table 2). The five elemental distribution maps on the right and below the SEM micrograph (Figure 6) were obtained by means of energy

PRE-PRINT ARTICLE

COPYRIGHT BY COMPOSITES THEORY AND PRACTICE JOURNAL

ISSN: 2299-128X

Polish Society of Composite Materials

dispersive X-ray spectroscopy (EDS) and illustrate the spatial distribution of specific elements within the observed microstructure.

The Al Kα1 map (cyan, top center in Figure 4) shows a widespread and intense signal, indicating that aluminum is the dominant element throughout the agglomerates. This confirms the presence of an Al_2O_3-based matrix. The Ni Kα1 map (yellow, bottom right in Figure 4) shows a significant and well-dispersed nickel signal overlapping with the alumina particles, suggesting that nickel is distributed relatively homogeneously throughout the composite. The clear presence of Ni supports its role as the metallic phase in the composite. The Fe Kα1 map (orange, bottom center in Figure 6) exhibits a weak, highly localized signal, indicating the presence of iron as a trace impurity or minor constituent, possibly originating from the nickel precursor or contamination during processing. The combined elemental map (bottom left in Figure 6) displays a superimposed image showing the distribution of all the mapped elements, Al (cyan), O (green), Ni (yellow) and Fe (orange), overlaid on the electron signal (gray). The overlay provides a comprehensive view of the phase distribution. Nickel is closely associated with the alumina agglomerates, while iron appears sparsely and is not co-located with the primary phases.

The elemental analysis confirms the presence of the NiAl + 30 wt% Al_2O_3 system, with nickel particles integrated into the alumina matrix. The co-localization of Al and O, combined with the significant Ni signal, suggests a successful composite structure. The minimal Fe content indicates that iron does not play a major role in the material's phase composition.

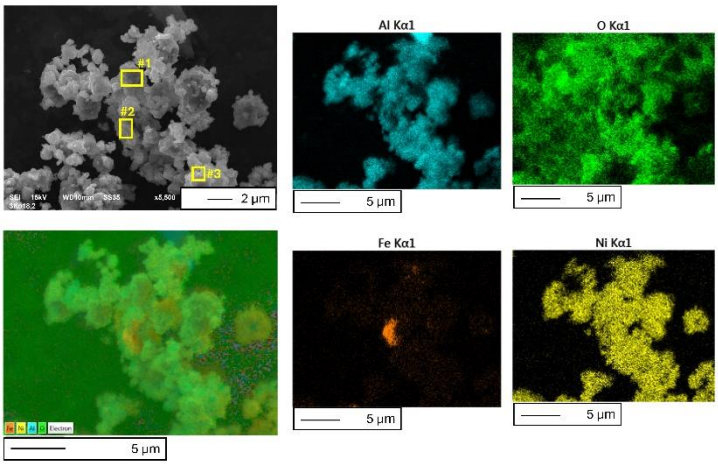

Figure 6. SEM micrographs and corresponding EDS elemental maps of NiAl + 30 wt% Al_2O_3 powder after mechanical alloying for 18 hours.

PRE-PRINT ARTICLE

COPYRIGHT BY COMPOSITES THEORY AND PRACTICE JOURNAL

ISSN: 2299-128X

Polish Society of Composite Materials

Table 2. EDS results for three areas (labelled #1, #2, and #3) shown in yellow squares in Figure 6.

NiAl + 30 wt% Al_2O_3 powder after mechanical alloying for 18 hours (Figure 6)	Area	Chemical composition							
		Aluminum		Oxygen		Nickel		Iron	
		Weight%	Atomic %	Weight%	Atomic %	Weight%	Atomic %	Weight%	Atomic %
	#1	20.60 ± 0.13	29.81 ± 0.02	9.74 ± 0.10	23.76 ± 0.23	67.22 ± 0.19	44.71 ± 0.12	2.45 ± 0.10	1.71 ± 0.07
	#2	20.65 ± 0.10	29.46 ± 0.07	9.73 ± 0.09	23.40 ± 0.05	25.51 ± 0.20	16.73 ± 0.12	44.11 ± 0.18	30.40 ± 0.10
	#3	36.27 ± 0.18	41.55 ± 0.12	17.71 ± 0.14	34.22 ± 0.15	46.02 ± 0.24	24.23 ± 0.06	-	-

In the first stage of the research on the obtained composites, the phase composition was examined in the raw state and after sintering. XRD patterns of the samples before (green body) and after sintering are displayed in Figures 7 and 8. Diffraction peaks of the Al_2O_3 and NiAl phases were present in the patterns of the green bodies (Figures 7a and 8a). Hence, during the mixing of the mechanically alloyed NiAl-30%Al_2O_3 pre-composite powder and Al_2O_3 powder in the PM400 planetary ball mill, no reaction between the components occurred. Nonetheless, in the patterns of the sintered samples (Figures 7 b and 8 b), diffraction peaks of Ni appeared next to the Al_2O_3 peaks.

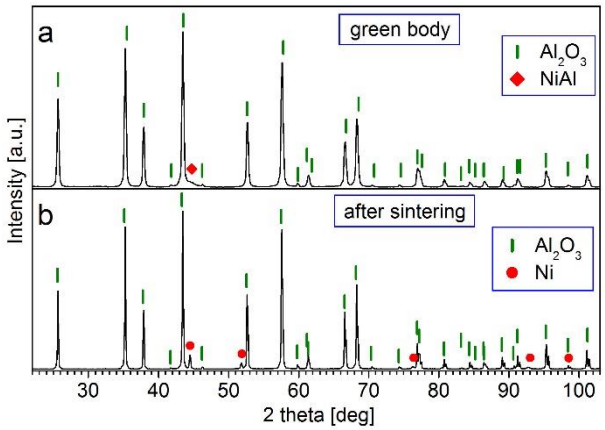

Figure 7. XRD patterns of Al_2O_3 + 2.5 vol.% of (NiAl + 30 wt% Al_2O_3) sample: (a) green body, (b) after sintering.

PRE-PRINT ARTICLE

COPYRIGHT BY COMPOSITES THEORY AND PRACTICE JOURNAL

ISSN: 2299-128X

Polish Society of Composite Materials

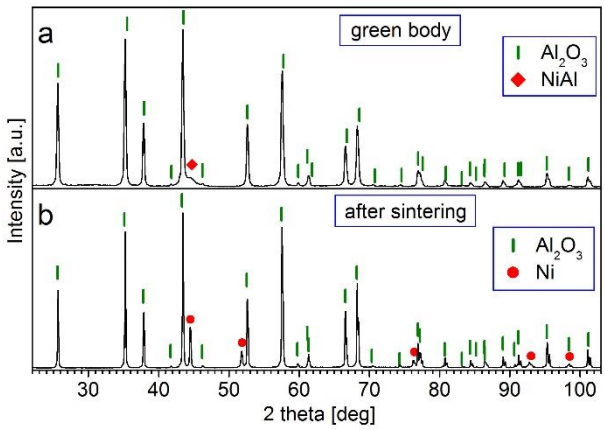

Figure 8. XRD patterns of Al_2O_3 + 5 vol.% of (NiAl + 30 wt% Al_2O_3) sample: (a) green body, (b) after sintering.

NiAl is stable only when sufficient aluminum remains in the intermetallic. Moreover, NiAl forms by means of a diffusion-driven reaction between Ni and Al during mechanical alloying. In the green bodies (Figs. 7a and 8a), the presence of this material is confirmed by XRD. However, at 1450°C, the stability of NiAl strongly depends on maintaining the correct stoichiometric activity of aluminum. If the activity of Al decreases, NiAl becomes thermodynamically unstable and decomposes according to reactions such as: NiAl → Ni + Al (released).

Additionally, in an N_2/H_2 atmosphere, aluminum is removed from NiAl due to reduction-driven volatilization. At 1450°C, aluminum is extremely reactive in a hydrogen-rich environment. It should be noted that several thermochemically favorable processes reduce the activity of Al within the composite, such as the formation and volatilization of aluminum-containing species and /or preferential stabilization of Al_2O_3, which consumes available Al.

In H_2, aluminum reacts to form volatile suboxides or hydrides, including: AlH_x species (gas phase), Al_2O (g) if even traces of oxygen are present or Al-containing hydroxides (in low oxygen partial pressures). These volatile species continuously remove Al from the NiAl lattice. Moreover, even ppm-level oxygen in the sintering chamber leads to the following reaction: Al (from NiAl) + H_2O / O_2 → Al_2O (g), AlOH (g), etc. Because they are gaseous, these products leave the material, reducing the activity of aluminum locally around the NiAl particles.

What is more, a large excess of ultrafine TM-DAR alumina surrounds the reinforcement particles. The Al in NiAl has a high affinity for oxygen and will preferentially diffuse toward the nearby Al_2O_3 surfaces where: Al (from NiAl) → Al^{3+} (incorporates into the Al_2O_3 lattice). This diffusion additionally lowers the activity of Al in NiAl.

PRE-PRINT ARTICLE

COPYRIGHT BY COMPOSITES THEORY AND PRACTICE JOURNAL

ISSN: 2299-128X

Polish Society of Composite Materials

It should be remembered that once the activity of Al falls below the NiAl stability threshold, NiAl decomposes. With Al being volatilized in the hydrogen atmosphere, possibly removed via hydroxylation or reduction reactions, and partially absorbed by the surrounding Al_2O_3, the NiAl phase is no longer stoichiometrically stable. Thus, NiAl undergoes disproportionation: NiAl → Ni (solid) + Al (lost/consumed). This explains why XRD detects Ni exclusively as the metallic phase in the sintered specimens.

A question arises: why are there no $NiAl_2O_4$ spinel forms (previous studies) [5, 13-15]? Earlier work showed that in air, NiAl oxidizes to the $NiAl_2O_4$ spinel [5, 13-15]. Under the present conditions, there is a strongly reducing atmosphere (H_2/N_2), and the partial pressure of oxygen is far below the threshold for spinel formation. Moreover, any oxygen present preferentially stabilizes Al_2O_3 rather than creates $NiAl_2O_4$. Therefore, spinels cannot form, and Ni remains as metallic Ni after NiAl decomposition.

During sintering at 1450°C in the reducing H_2/N_2 atmosphere, the NiAl intermetallic phase decomposes because aluminum is thermodynamically unstable under these conditions. Hydrogen promotes the volatilization of Al-Al-containing species and/or the diffusion of Al toward the Al_2O_3 matrix, thereby lowering the activity of aluminum below that required for NiAl stability. As a result, NiAl decomposes into metallic Ni, which is detected in the XRD patterns, while no $NiAl_2O_4$ spinel forms owing to the strongly reducing environment.

Figure 9 shows the distribution maps of individual elements in the produced composites. Moreover, in Figure 9, two additional measurement areas, #1 and #2, are marked for each series to determine the elemental composition. Table 3 presents the chemical composition of selected points in Figure 9. The results are given in weight percentage (wt%) and atomic percentage (at.%) for the following elements: aluminum (Al), oxygen (O), nickel (Ni), and iron (Fe).

The presence of Ni-rich regions confirms the distribution of nickel aluminide within the composite. A small percentage of iron (Fe) was detected, likely originating from contamination or impurities in the raw materials.

The comparison between Figure 9(a) and Figure 9(b) reveals that increasing the NiAl content from 2.5 vol.% to 5 vol.% does not significantly affect the distribution of the major phases but does influence the overall composition. This analysis provides a structured interpretation of the EDX results, showing the phase distribution and confirming the presence of nickel aluminide within the alumina matrix.

PRE-PRINT ARTICLE

COPYRIGHT BY COMPOSITES THEORY AND PRACTICE JOURNAL

ISSN: 2299-128X

Polish Society of Composite Materials

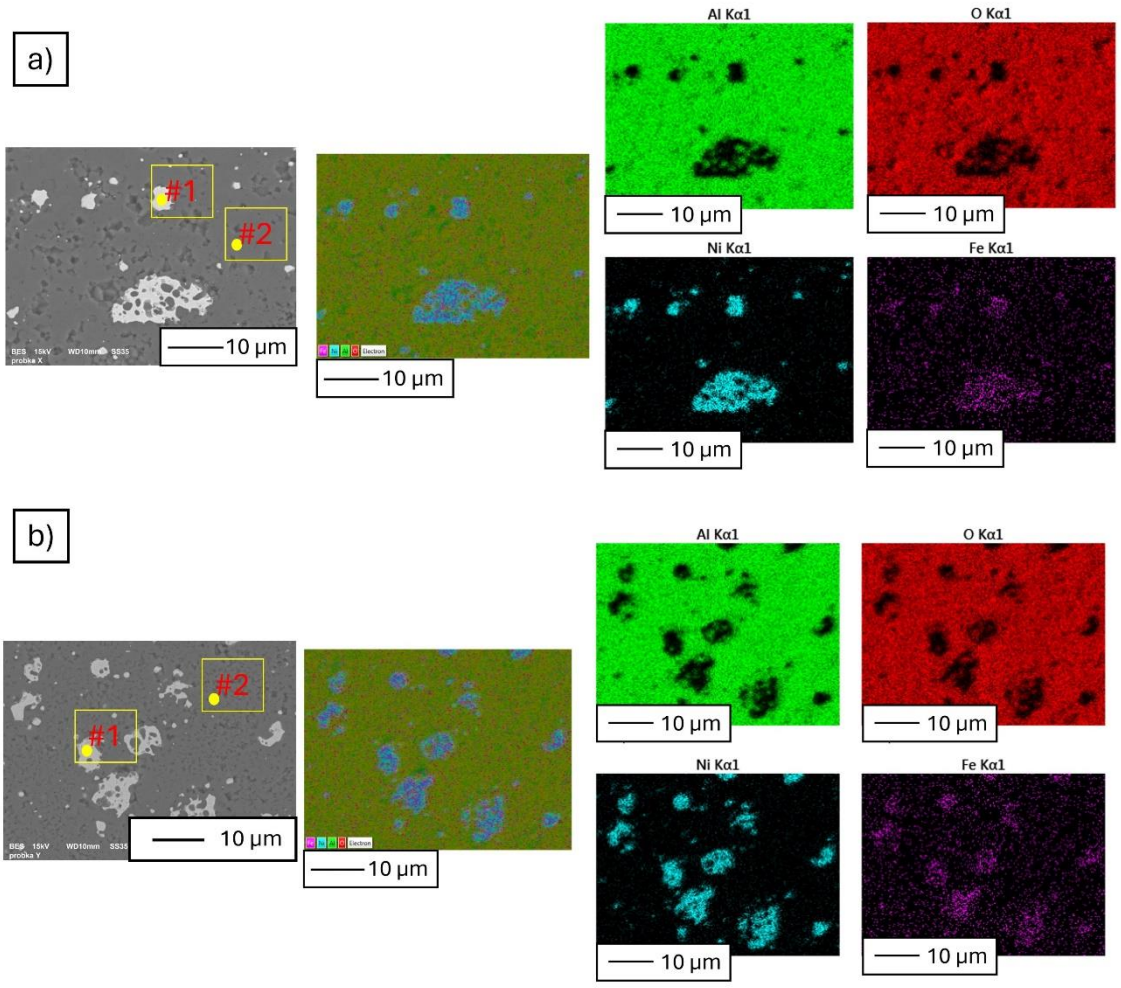

Figure 9. Analysis of composite chemical composition: a) Series I – Al_2O_3 + 2.5 vol.% of (NiAl + 30 wt% Al_2O_3), b) Al_2O_3 + 5 vol.% of (NiAl + 30 wt% Al_2O_3).

PRE-PRINT ARTICLE
COPYRIGHT BY COMPOSITES THEORY AND PRACTICE JOURNAL
ISSN: 2299-128X
Polish Society of Composite Materials

Table 3. Chemical composition of samples (Fig. 9) determined by EDX analysis

Sample	Point [Figure 9]	Chemical composition							
		Aluminum		Oxygen		Nickel		Iron	
		Weight%	Atomic %	Weight%	Atomic %	Weight%	Atomic %	Weight%	Atomic %
Figure 9 a)	#1	2.5 ± 0.07	5.28 ± 0.02	-	-	94.94 ± 0.12	92.11 ± 0.03	2.56 ± 0.10	2.61 ± 0.07
Figure 9 a)	#2	54.05 ± 0.13	41.09 ± 0.09	49.95 ± 0.13	58.91 ± 0.11	-	-	-	-
Figure 9 b)	#1	-	-	-	-	94.47 ± 0.10	97.34 ± 0.08	2.53 ± 0.10	2.66 ± 0.09
Figure 9 b)	#2	53.04 ± 0.09	42.08 ± 0.04	46.96 ± 0.03	57.92 ± 0.09	-	-	-	-

The Ni and Fe maps in Fig. 9 do not imply a separate Fe-bearing crystalline phase that would contradict the XRD pattern. The Fe signal is most likely a trace contamination (originating from the milling media or raw powders, as noted earlier) and/or Fe dissolved in the Ni-rich regions as a substitutional solid solution. At the sintering temperature (1450°C), Fe and Ni are essentially miscible, and any Fe present will be incorporated into the Ni lattice (or present as very small/poorly crystalline particles), and therefore will not produce a distinct XRD phase separate from Ni. Additionally, local EDS can overrepresent small Fe-rich inclusions or surface contamination that are below the XRD detection limit (typically approximately 2-5 wt% for well-crystallized phases). It should be noted that EDS is a local and qualitative technique, whereas XRD is a bulk technique with a detection limit.

EDS in SEM gives local elemental maps (spot or area) and is very sensitive to small, localized enrichments or surface contaminants. It can show strong signals from tiny particles or thin surface layers. XRD detects bulk crystalline phases and typically cannot detect phases present at concentrations below a few weight percent (often quoted as 2-5 wt%, depending on the crystallinity, peak overlap, and instrument settings). Thus, tiny Fe-rich inclusions or Fe in a solid solution will not produce a separate XRD peak. Ni and Fe are mutually soluble over a wide composition range at high temperature. This will appear in XRD as the Ni phase, not as an extra Fe phase. At the scale of conventional XRD, the Ni peaks will therefore absorb any Fe signal.

PRE-PRINT ARTICLE

COPYRIGHT BY COMPOSITES THEORY AND PRACTICE JOURNAL

ISSN: 2299-128X

Polish Society of Composite Materials

To sum up, the weak Fe signal in the EDS maps most likely originates from trace contamination introduced during mechanical alloying (the milling media or powder impurities) and/or from Fe dissolved in the Ni lattice. At 1450°C, Fe and Ni are mutually soluble, so any Fe is expected to be incorporated into the Ni-rich regions (or present as nanoscale inclusions below XRD detection limits), which explains why the XRD pattern shows only the Ni metallic phase and no separate Fe-rich crystalline phase.

The results indicate that the hardness of the composites decreased with an increase in the content of the NiAl-30Al_2O_3 pre-composite powder. Specifically, Series I, with 2.5 vol.% NiAl-30Al_2O_3, exhibited a higher hardness (17.01 ± 0.61 GPa) compared to Series II, which had 5 vol.% and a hardness of 15.73 ± 1.51 GPa. This trend can be attributed to the higher volume fraction of the metallic phase (NiAl) in Series II, which typically exhibits lower hardness than the ceramic phase (Al_2O_3). The soft metallic regions reduce the overall resistance to deformation under applied loads, thereby decreasing the composite hardness.

The fracture toughness values, however, did not show significant differences between the two series. Series I displayed a fracture toughness of 5.14 ± 0.30 MPa·$m^{0.5}$, while Series II had a slightly higher value of 5.20 ± 0.37 MPa·$m^{0.5}$. This suggests that the increase in the NiAl content slightly improved the material's ability to resist crack propagation. Typical impressions after hardness measurements of the produced composites are shown in Figure 10. The fracture toughness values of Series I and Series II are nearly identical because the increase in the metallic phase content from 2.5 to 5 vol.% is insufficient to significantly alter the crack-interaction mechanisms that govern toughening in alumina-based composites. After sintering in H_2/N_2, the reinforcement exists as isolated Ni particles that provide only modest toughening and do not form effective crack-bridging ligaments or strong deflection sites. Moreover, the Al_2O_3 grain size and matrix microstructure are similar in both composites, and the absence of $NiAl_2O_4$ spinel, known to enhance toughness in air-sintered systems, further limits toughening. Consequently, both materials exhibit comparable fracture toughness despite the differences in their metallic content.

PRE-PRINT ARTICLE

COPYRIGHT BY COMPOSITES THEORY AND PRACTICE JOURNAL

ISSN: 2299-128X

Polish Society of Composite Materials

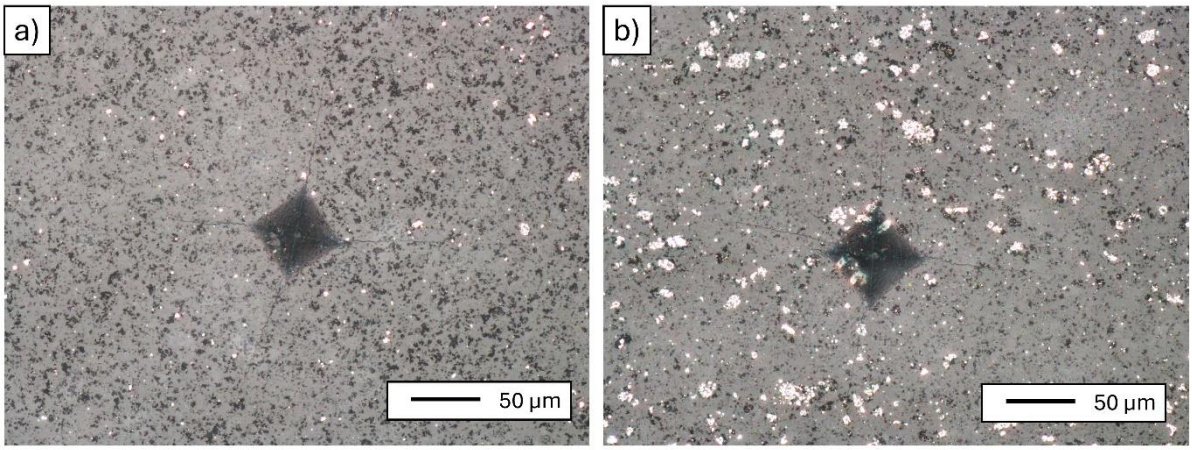

Figure 10. Examples of impressions after hardness measurement of produced composites.

The tests revealed that sample Series I (Figure 11a) exhibits very high hardness. It withstood a load of 25 kN. On the other hand, sample Series II (Figure 11b) transferred a load of only 17 kN. Neither Series I nor II exhibit unevenness in the formation of deformations during loading. The samples are very hard and coherent. They show no changes in the deformation fields. The cracks occur dynamically in both the tested series. The prevailing load did not weaken the samples during the test. The destruction occurred in the zones along the loading axis, leaving a core that transferred the main load. This indicates the material's high cohesion. Both samples (selected from individual series) were still able to transfer a correspondingly smaller load after being damaged by the crack. This is difficult to explain because, despite the brittle cracking that is clearly evident, the sample continues to transfer loads. It gives the impression that the load which occurs strengthens the load zone.

PRE-PRINT ARTICLE

COPYRIGHT BY COMPOSITES THEORY AND PRACTICE JOURNAL

ISSN: 2299-128X

Polish Society of Composite Materials

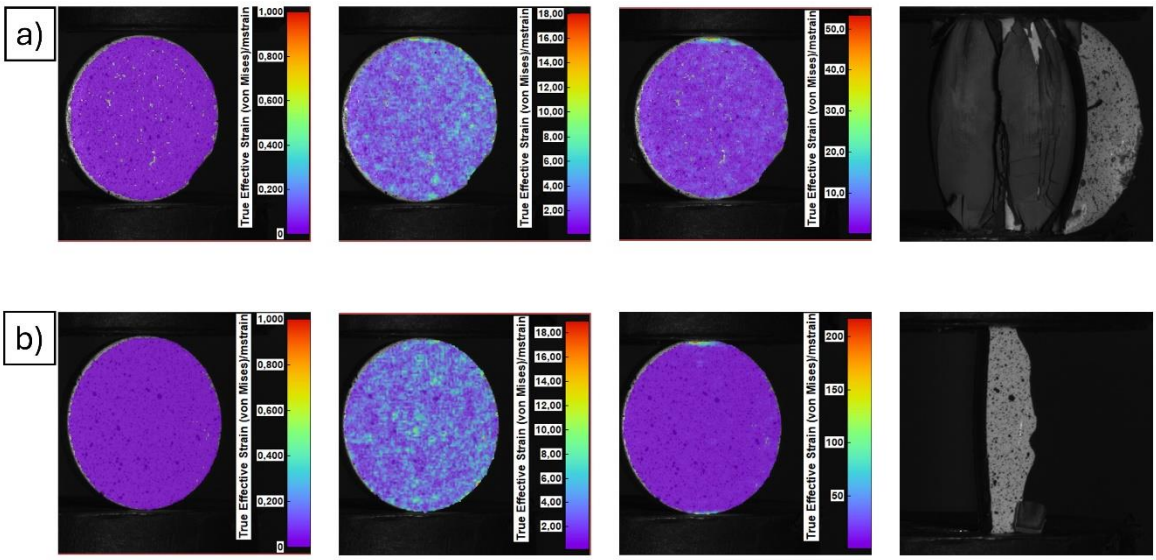

Figure 11. Representative strain distribution in composites obtained by DIC technique: a) Series I – Al_2O_3 + 2.5 vol.% (NiAl + 30 wt.% Al_2O_3), b) Series II – Al_2O_3 + 5 vol.% (NiAl + 30 wt% Al_2O_3).

Figure 12 presents the force-displacement curves as a result of compression tests for two composite series: Series I (orange curve) and Series II (green curve). In both cases, the loading behavior up to failure exhibits an initially elastic character, a nearly linear increase in force with small displacement, indicating high material stiffness. Only the force displacement curves are presented in Fig. 12 because the brittle fracture of the composites leads to non-uniform deformation and fragmentation during loading. Under these conditions, the instantaneous load-bearing cross-section and effective gauge length cannot be reliably defined, making conventional engineering stress-strain calculations invalid. Therefore, force and displacement, the directly measured quantities, are used to characterize the compressive response, while the DIC strain maps provide local deformation information. The maximum load-bearing capacity (compressive force) is clearly higher for the composite with the lower metallic phase content (Series I), which reaches approximately 13.7 kN, whereas Series II peaks at around 1 kN. This indicates that the samples with 2.5 vol.% NiAl withstand significantly higher compressive loads than those with 5 vol.% NiAl. The curve for Series I reaches a higher maximum and is steeper, suggesting slightly higher effective stiffness for the composite with the lower metal content. The Series II curve peaks at a lower force and exhibits a more gradual slope, indicating greater material compliance (lower stiffness) with the higher NiAl content. Both series exhibit elastic behavior up to crack initiation; no extended plastic plateau is observed, and after reaching the maximum load, the samples fail abruptly. In Series I, the force drop on the curve is almost vertical (a sudden, catastrophic failure occurs at approximately 0.33 mm), whereas in Series II, the curve shows slight flattening near the peak (around 0.27 mm), followed by a force drop. This suggests a somewhat less violent fracture in the material with the higher NiAl content – the

PRE-PRINT ARTICLE
COPYRIGHT BY COMPOSITES THEORY AND PRACTICE JOURNAL
ISSN: 2299-128X
Polish Society of Composite Materials

Series II sample gradually loses its load-bearing capacity after reaching the maximum, rather than undergoing immediate complete failure. This observation aligns with the finding that, after crack initiation, the material continued to carry a portion of the load. Overall, however, both composites exhibit limited plasticity after reaching the peak force; the structure undergoes extensive cracking and load reduction.

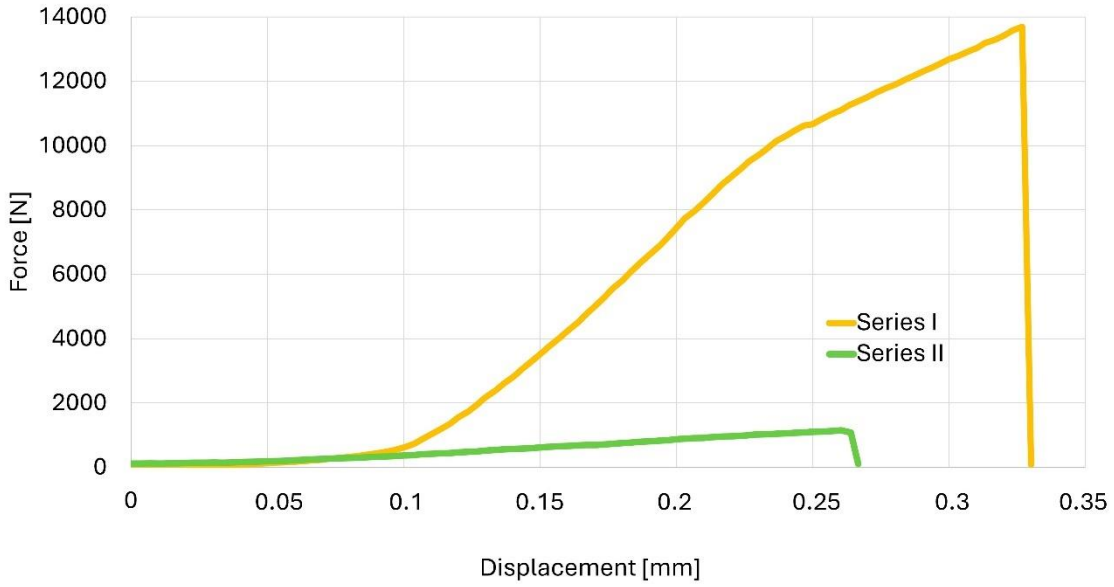

Figure 12. Deformation as a result of monotonic compression: a) Series I – Al_2O_3 + 2.5 vol.% (NiAl + 30 wt% Al_2O_3), b) Series II – Al_2O_3 + 5 vol.% (NiAl + 30 wt% Al_2O_3).

The significantly lower and nearly constant load-bearing capacity observed in Series II arises from its higher content of the metallic Ni-rich phase. The increased fraction of soft Ni regions disrupts the continuity of the Al_2O_3 matrix, reduces the composite's effective stiffness, and creates additional weak interfaces that promote early crack initiation. As a result, Series II reaches peak load much earlier and at a markedly lower force. After initial cracking, the specimen retains only limited load-transfer capacity, leading to the characteristic flat post-peak plateau associated with frictional contact between fragmented regions. In Series I, the lower metal content preserves the integrity of the ceramic skeleton, allowing it to sustain much higher loads before catastrophic failure.

In the next step, stereological analysis was performed, based on which the influence of the NiAl + 30 wt% Al_2O_3 phase content on Al_2O_3 grain growth was determined. Both histograms present the volume-based particle size distributions (d_2) of the composite powders as measured, expressed as percentages across the particle size intervals. In Series I (Figure 13a), the particle size distribution spans from approximately 0.2 µm to 5.4 µm, with the majority of particles concentrated between 0.8 µm and 2.4 µm. The distribution shows a

PRE-PRINT ARTICLE
COPYRIGHT BY COMPOSITES THEORY AND PRACTICE JOURNAL
ISSN: 2299-128X
Polish Society of Composite Materials

slightly right-skewed profile, peaking at 1.2-1.4 μm, with a maximum frequency of around 10%. The calculated mean particle size (d_2, averaged) is 1.49 ± 0.82 μm, indicating a moderately broad distribution, with some particles up to ~5 μm. In Series II (Figure 13b), the overall distribution is very similar in shape and range, spanning 0.2 μm to ~5.4 μm, with the majority of particles also located within the 0.8 μm to 2.4 μm interval. The histogram similarly peaks at around 1.2-1.4 μm, with approximately 11% frequency, suggesting a comparable dominant particle size. The calculated average particle size is 1.47 ± 0.81 μm, nearly identical to Series I, again showing a relatively broad distribution with a long tail toward larger particle sizes.

Despite the difference in the volume content of the (NiAl + 30 wt% Al_2O_3) phase (2.5 vol.% in Series I vs. 5 vol.% in Series II), the particle size distribution remains effectively unchanged. The similarity in both the mean and standard deviation values confirms that the increase in volume fraction does not significantly affect the particle size distribution, which is critical for maintaining a uniform microstructure and reproducible properties in the final sintered composite.

Although Series I and Series II contain different amounts of the reinforcement phase (2.5 vs. 5 vol.% of NiAl + 30 wt.% Al_2O_3), the particle size distribution of this phase remains nearly unchanged (Fig. 13). This observation arises from several key factors intrinsic to the processing route. Firstly, mechanical alloying fixes the particle size before composite fabrication; moreover, slip casting mixes but does not fragment or grow reinforcement particles. What is more, sintering at 1450°C in H_2/N_2 does not promote coarsening of the Ni-rich particles. The reinforcing phase (NiAl + 30 wt.% Al_2O_3) is produced by high-energy mechanical alloying, which refines and homogenizes the particle size, stabilizes the nanocrystalline NiAl domains within the submicron Al_2O_3 clusters, and establishes a well-defined and narrow particle size distribution. The composite inherits this size distribution. Adding more reinforcement powder only changes the particle count, not their size. Slip casting incorporates the pre-composite powder into the ceramic slurry, but it does not separate, grind, or coarsen the reinforcing particles.

The homogenization in the planetary mixer maintains their existing size, and agglomerates are broken down uniformly, independent of the volume fraction. Therefore, Series I and Series II begin the sintering stage with identically sized reinforcement particles. During sintering, NiAl decomposes into metallic Ni, which remains isolated within the alumina matrix. Ni does not undergo Ostwald ripening or coalescence because Al_2O_3 physically separates the metal particles; Thus, the reinforcement does not grow or shrink significantly during sintering in either series. The ultrafine Al_2O_3 (TM-DAR) matrix densifies quickly at 1450°C. Once densification begins, the matrix "locks in" the Ni-rich particles, preventing their mobility and restricting coarsening by limiting diffusion pathways. Because both series employ the same matrix and sintering protocol, they exhibit nearly identical grain boundary mobility and, consequently, similar particle sizes. In Series II, there are more particles of the reinforcement, but their size distribution is preserved. The histogram shows

PRE-PRINT ARTICLE

COPYRIGHT BY COMPOSITES THEORY AND PRACTICE JOURNAL

ISSN: 2299-128X

Polish Society of Composite Materials

more counts in Series II, while the peak position, width, and shape remain essentially unchanged. This is exactly what is expected when the particle size is set prior to consolidation.

Summarizing the above considerations regarding the particle size distribution in both series, despite the higher content of reinforcing phase in Series II, the particle size distributions of the NiAl + Al_2O_3 particles remained almost identical to those of Series I (Fig. 13). This results from the fact that the particle size is determined during the mechanical alloying stage. The subsequent processing steps, such as slip casting, drying, and sintering, do not significantly alter the particle size. The alumina matrix rapidly densifies during sintering and restricts the mobility of the Ni-rich particles, preventing coarsening. Therefore, increasing the reinforcement volume fraction increases the number of particles in the composite but does not affect their size, resulting in nearly identical particle size distributions in both series.

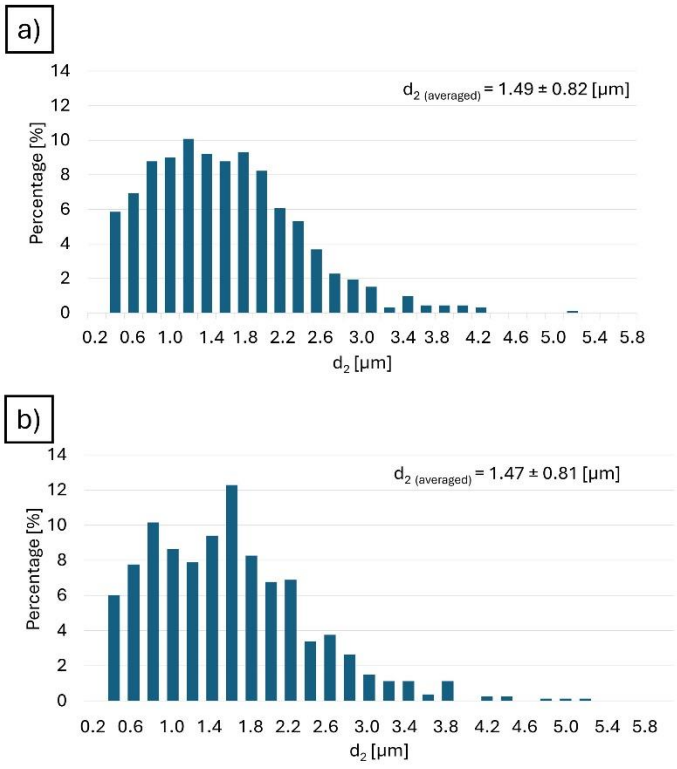

Figure 13. Particle size distribution histograms of Al_2O_3 in composites: a) Series I – Al_2O_3 + 2.5 vol.% (NiAl + 30 wt% Al_2O_3), b) Series II – Al_2O_3 + 5 vol.% (NiAl + 30 wt% Al_2O_3).

PRE-PRINT ARTICLE

COPYRIGHT BY COMPOSITES THEORY AND PRACTICE JOURNAL

ISSN: 2299-128X

Polish Society of Composite Materials

Conclusions

This study explores the fabrication and properties of Al_2O_3-based composites reinforced with NiAl + 30 wt% Al_2O_3 powder produced by mechanical alloying. The composites were shaped by slip casting and sintered at 1450°C in a reducing N_2/H_2 atmosphere. Two material series were prepared, containing 2.5 vol.% and 5 vol.% of the reinforcement phase.

X-ray diffraction analysis showed that before sintering, the composites contained NiAl and Al_2O_3. After sintering in the reducing atmosphere, Ni was detected instead of NiAl, and importantly, no $NiAl_2O_4$ spinel phase was formed. SEM/EDS studies confirmed uniform distribution of Ni-rich regions within the alumina matrix, and grain size analysis showed similar Al_2O_3 grain sizes in both series.

Mechanical testing revealed that the hardness decreased with a higher reinforcement content: about 17.0 GPa for 2.5 vol.% and 15.7 GPa for 5 vol.%. The fracture toughness values remained nearly constant at ~5.1 - 5.2 $MPa \cdot m^{0.5}$, showing no significant improvement compared to monolithic alumina. The compression tests indicated high cohesion and brittle failure, with maximum loads of about 25 kN for the lower reinforcement content and 17 kN for the higher content. Interestingly, even after cracking, the samples continued to carry part of the load.

The contribution of this research lies in demostrating how the sintering atmosphere influences phase evolution and mechanical behavior. In contrast, in air-sintered composites, NiAl transforms into $NiAl_2O_4$ spinel (which enhances toughness), whereas reducing conditions suppress spinel formation and stabilize metallic Ni. This distinction highlights the key role of $NiAl_2O_4$ in toughening mechanisms.

The study also introduces new compressive-strength data, providing a broader view of the mechanical performance of Al_2O_3-NiAl composites. Overall, it demonstrates that controlling the sintering atmosphere is an effective strategy for tailoring the microstructure and mechanical properties of ceramic–intermetallic composites.

This research is significant because it shows that the sintering atmosphere is a decisive factor in phase formation and toughening mechanisms in Al_2O_3-NiAl composites. It introduces new compressive-strength data, demonstrates the mechanical consequences of suppressing spinel, and clarifies how reinforcement content influences hardness-versus-toughness trade-offs. The study adds an important dimension to the understanding of processing structure property relationships in ceramic intermetallic systems, relevant to aerospace, automotive, and energy applications where high strength and toughness are critical.

PRE-PRINT ARTICLE

COPYRIGHT BY COMPOSITES THEORY AND PRACTICE JOURNAL

ISSN: 2299-128X

Polish Society of Composite Materials

Declaration of interest statement

The authors declare that they have no known competing financial interests or personal relationships that could have influenced the work reported in this paper. On behalf of all the authors, the corresponding author states that there is no conflict of interest.

Funding

The research was funded by POB Technologie Materiałowe of Warsaw University of Technology within the Excellence Initiative: Research University (IDUB) programme. Manager: Professor Katarzyna Konopka.

References

[1] W.G. Fahrenholtz, D.T. Ellerby and R.E Loehman: *Ceramic-Metal and Ceramic-Intermetallic Composites by Reactive Processing*, *24th Annual Conference on Composites, Advanced Ceramics, Materials, and Structures: A: Ceramic Engineering and Science Proceedings* 2000, https://doi.org/10.1002/9780470294628.ch79

[2] C.M. Ward-Close, R. Minor and P.J. Doorbar: *Intermetallics*, 1996, vol. 4, pp. 217-229. https://doi.org/10.1016/0966-9795(95)00037-2.

[3] C. Senderowski C: *Materials*, 2022, vol. 15, pp. 8408. https://doi.org/10.3390/ma15238408

[4] T. Klassen, R. Günther, B. Dickau, F. Gärtner, A. Bartels, R. Bormann and H. Mecking: *J. Am. Ceram. Soc.*, 1998, vol. 81, pp. 2504-2506. https://doi.org/10.1111/j.1151-2916.1998.tb02654.x

[5] J. Zygmuntowicz, K. Konopka, M. Krasnowski et al.: *Metall. Mater. Trans. A*, 2025, vol. 55, pp. 5160–5176. https://doi.org/10.1007/s11661-024-07600-8

[6] D. Oleszak: *J. Mater. Sci.*, 2004, vol. 39, pp. 5169–5174.

[7] D.R. Leiva, E.M.J.A. Pallone, R. Tomasi and W.J. Botta Filho: *Mater. Sci. Forum*, 2003, vol. 416–418, pp. 493–498. https://doi.org/10.4028/www.scientific.net/msf.416-418.493

[8] A. Dolata-Grosz, B. Formanek, J. Śleziona and J. Wieczorek: *J. Mater. Process. Technol*., 2005, vol. 162–163, pp. 33–38. https://doi.org/10.1016/j.jmatprotec.2005.02.009.

[9] K. Konopka: *J. Compos. Sci*., 2022, vol. 6, p. 178. https://doi.org/10.3390/jcs6060178

[10] CC. Tekoğlu, Ş. Çelik, H. Duran, M. Efe, S. Baier-Stegmaier and K.L. Nielsen: *Eng. Fract. Mech*., 2021, vol. 253, pp. 107901. https://doi.org/10.1016/j.engfracmech.2021.107901.

[11] O. Gavalda-Diaz, E. Saiz, J. Chevalier and F. Bouville: *Int. Mater. Rev*., 2025, vol. 70, pp. 3–30. https://doi.org/10.1177/09506608241308337

[12] A. Knaislová, J. Linhart, P. Novák et al.: *Powder Metall*., 2019, vol. 62, pp. 54–60. https://doi.org/10.1080/00325899.2019.1569812

[13] J. Zygmuntowicz, K. Konopka, M. Krasnowski, P. Piotrkiewicz, M. Wachowski, R. Żurowski, K. Cymerman, K. Kulikowski and R. Sobiecki: *Materials*, 2023, vol. 16, pp. 4136. https://doi.org/10.3390/ma16114136

[14] K. Konopka, J. Zygmuntowicz, M. Krasnowski, K. Cymerman, M. Wachowski and P. Piotrkiewicz: *Materials*, 2022, vol. 15, pp. 407. https://doi.org/10.3390/ma15020407

[15] K. Konopka, M. Krasnowski, J. Zygmuntowicz, K. Cymerman, M. Wachowski and P. Piotrkiewicz: *Materials*, 2021, vol. 14, pp. 3398. https://doi.org/10.3390/ma14123398

[16] S. Marimuthu, A.C.J. Malathi, V. Raghavan and A.N. Grace: *Advanced Ceramics for Energy Storage*, *Thermoelectrics and Photonics*, Elsevier, 2023, pp. 19–39. https://doi.org/10.1016/B978-0-323-90761-3.00018-8.

[17] J. Guo, J. Li, H. Kou, *Chapter 19 - Chemical Preparation of Advanced Ceramic Materials*, *Modern Inorganic Synthetic Chemistry*, Elsevier, 2011, pp 429-454, https://doi.org/10.1016/B978-0-444-53599-3.10019-8.

[18] A. Michalski and M. Rosiński: *J. Am. Ceram. Soc*., 2008, vol. 91, pp. 3560–3565. https://doi.org/10.1111/j.1551-2916.2008.02738.x

[19] A. Michalski and D. Siemiaszko: *Int. J. Refract. Met. Hard Mater*., 2007, vol. 25, pp. 153–158. https://doi.org/10.1016/j.ijrmhm.2006.03.007.

[20] B. Saleh, J. Jiang, R. Fathi, T. Al-hababi, Q. Xu, L. Wang, D. Song and A. Ma: *Compos. Part B Eng.*, 2020, vol. 201, pp. 108376. https://doi.org/10.1016/j.compositesb.2020.108376.

[21] E. Baseta, M. Palma, F. Heher, T. Konegger and M. Kaftan: *Ceramics*, 2025, vol. 8, pp. 6. https://doi.org/10.3390/ceramics8010006

[22] V.P. Meshalkin and A.V. Belyakov: *Processes*, 2020, vol. 8, pp. 1004. https://doi.org/10.3390/pr8081004

[23] R.I. Shakirzyanov, N.O. Volodina, Y.A. Garanin et al.: *Discov. Mater*., 2024, vol. 4, pp. 48. https://doi.org/10.1007/s43939-024-00123-4

[24] I. Parchovianská, M. Parchovianský, A. Nowicka, A. Prnová, P. Švančárek and A. Pakseresht: *J. Mater. Res. Technol*., 2023, vol. 24, pp. 4573–4586. https://doi.org/10.1016/j.jmrt.2023.04.054.

[25] J. Zygmuntowicz, P. Wiecińska, A. Miazga et al.: J. *Therm. Anal. Calorim*., 2016, vol. 125, pp. 1079–1086. https://doi.org/10.1007/s10973-016-5357-2

[26] J. Zygmuntowicz, K. Konopka, M. Krasnowski, P. Piotrkiewicz, J. Bolek, M. Wachowski, R. Żurowski and M. Szafran: *Materials*, 2022, vol. 15, pp. 2920. https://doi.org/10.3390/ma15082920

[27] *ASTM D3766-08*; Standard Terminology Relating to Catalysts and Catalysis. ASTM International: West Conshohocken, PA, USA; Philadelphia, PA, USA, 2018.

[28] Suryanarajana, C.; *Grant Norton, M. X-ray Diffraction. A Practical Approach*; Springer Science+Business Media: New York, NY,USA, 1998.

[29] V. Mote, Y. Purushotham and B. Dole: *J. Theor. Appl. Phys*., 2012, vol. 6, pp. 6. https://doi.org/10.1186/2251-7235-6-6

[30] S. Devesa, A.P. Rooney, M.P. Graça, D. Cooper and L.C. Costa: *Mater. Sci. Eng. B*, 2021, vol. 263, pp. 114830. https://doi.org/10.1016/j.mseb.2020.114830.

[31] V.S. Vinila and J. Isac: *Design, Fabrication, and Characterization of Multifunctional Nanomaterials*, Elsevier, 2022, pp. 319–341. https://doi.org/10.1016/B978-0-12-820558-7.00022-4.

[32] ISO 6507-1:2018(E), Metallic materials - Vickers hardness test - Part 1: Test method. Międzynarodowa Organizacja Normalizacyjna, 2018.

[33] Y. Guo, T. Staedler, J. Müller, S. Heuser, B. Butz, X. Jiang, A detailed analysis of the determination of fracture toughness by nanoindentation induced radial cracks, *Journal of the European Ceramic Society*, 2020, vol. 40, 2, pp. 276-289, https://doi.org/10.1016/j.jeurceramsoc.2019.10.013.

[34] G. Anstis, P. Chantikul, B. Lawn and D.A. Marshall: *J. Am. Ceram. Soc*., 1981, vol. 64, pp. 533–538.

[35] T. Wejrzanowski, W. Spychalski, K. Rożniatowski and K. Kurzydłowski: *Int. J. Appl. Comput. Math*., 2008, vol. 18, pp. 33-39. https://doi.org/10.2478/v10006-008-0003-1.

[36] T. Wejrzanowski and K.J. Kurzydlowski: *Solid State Phenom*., 2003, vol. 94, pp. 221–228. https://doi.org/10.4028/www.scientific.net/SSP.94.221.

[37] J. Michalski, T. Wejrzanowski, R. Pielaszek, K. Konopka, W. Łojkowski and K.J. Kurzydłowski: *Mater. Sci. Pol*., 2005, vol. 23, pp. 79–86.

[38] K.J. Kurzydlowski and B. Ralph: The Quantitative Description of the Microstructure of Materials, *CRC Press*, 1995.